

Potential Barrier Height at the Grain Boundaries of Poly-Silicon Nanowire

Assaf Shamir^{1,†}

¹Department of Physical Electronics, School of Electrical Engineering, Tel-Aviv University, Ramat-Aviv 69978, Israel.

E-mail: assafshamir@mail.tau.ac.il

Iddo Amit^{1,†}

¹Department of Physical Electronics, School of Electrical Engineering, Tel-Aviv University, Ramat-Aviv 69978, Israel.

E-mail: iddoamit@post.tau.ac.il

Danny Englander¹

¹Department of Physical Electronics, School of Electrical Engineering, Tel-Aviv University, Ramat-Aviv 69978, Israel.

E-mail: dengland46@gmail.com

Dror Horvitz¹

¹Department of Physical Electronics, School of Electrical Engineering, Tel-Aviv University, Ramat-Aviv 69978, Israel.

E-mail: dror.horvitz@fei.com

Yossi Rosenwaks

¹Department of Physical Electronics, School of Electrical Engineering, Tel-Aviv University, Ramat-Aviv 69978, Israel.

E-mail: yossir@eng.tau.ac.il, yossir@eng.tau.ac.il

[†] These authors contributed equally to this work

Abstract. We present measurements of the potential barrier height and its dependence on grain size, in poly-silicon nanowire (P-SiNW) arrays. Measurements conducted using Kelvin probe force microscopy coupled with electrostatic simulations, enabled us also to extract the density of grain boundary interface states and their energy distribution. In addition it was shown that the barrier height scales with the grain size as the square of the grain radius.

Keywords: Nanowires, Grain boundaries, Potential Barrier, Polycrystalline silicon, Kelvin probe force microscopy. Submitted to: *Nanotechnology*

1. Introduction

Over the past two decades, silicon nanowires (SiNWs) have emerged as important candidates for future microelectronics, solar cells and bio- and chemical sensors.[1, 2, 3, 4] There are two major approaches for fabricating nanostructured devices, the top-down and the bottom up approach. Bottom-up approaches, which usually involve metal-catalyzed,[5, 6] or auto-catalyzed self-assembled nanowire growth,[7, 8] benefit from a good control over the growth conditions and large versatility in shape, size, and the materials in use. Moreover, the bottom-up fabrication process produces uniformly-sized, single crystalline nanowires. However, one of the major obstacles with catalytic growth is the challenge of integrating nanowires into a functional device, as for most growth methods, the nanowires grow at random locations. The top-down approach overcomes these shortcomings by using various advanced methods such as deep UV lithography, which has the advantage of being a complementary metal-oxide-semiconductor (CMOS) compatible technique, and show excellent electrical properties of single-crystalline silicon nanowires for biosensing.[2, 9, 10] A disadvantage of the top down approach is that the use of high-quality silicon-on-insulator (SOI) wafers results in a costly production process, unsuitable for disposable sensor production. Recently, a low cost, top-down approach of poly-crystalline silicon nanowires (P-SiNWs) synthesis was demonstrated, using a classical fabrication method commonly used in microelectronic industry – the so-called sidewall spacer technique.[11, 12, 13, 14] This top-down approach was previously demonstrated as a good method for biosensor fabrication for several analytes, all in which, a detection limit of femto-molar (fM) level was observed.[15, 1, 16, 17]

The main difference between single crystalline silicon (SC-Si) and poly crystalline silicon (PC-Si) is charge trapping at Grain Boundaries (GBs) in the latter. Therefore, a design of a polycrystalline device requires information of the density and energy-distribution of the GB interface states (GBIS), and the grain size and its ramifications on the corresponding potential barrier height.

J. Y. Seto showed using a simple model that the presence of trapping states at GBs affects the Si conductivity by reducing carrier mobility. Following the capture of mobile carriers, the traps become electrically charged, forming a space charge region and a potential energy barrier, which impedes the motion of mobile carriers from one crystallite to another, thus reducing their mobility.[18] Amit *et al.* have recently measured the interface states energy distribution in P-SiNW arrays which were fabricated in a similar manner to the wires measured in this work. Using numerical electrostatic simulations, the GBIS distribution was determined to have a ‘U’-shape distribution within the energy gap.[14] However, these results were based on a mean-distribution approach for GB simulations, which was used to simplify the complexity involved in introducing a polycrystalline material into a technology computer aided design (TCAD) simulation. The GBIS characteristics are crucial for the design of a P-Si based device, since the trapping of free carriers at the interface states results in a critical level of doping, below which the silicon becomes fully depleted. We present here measurements of the potential barrier

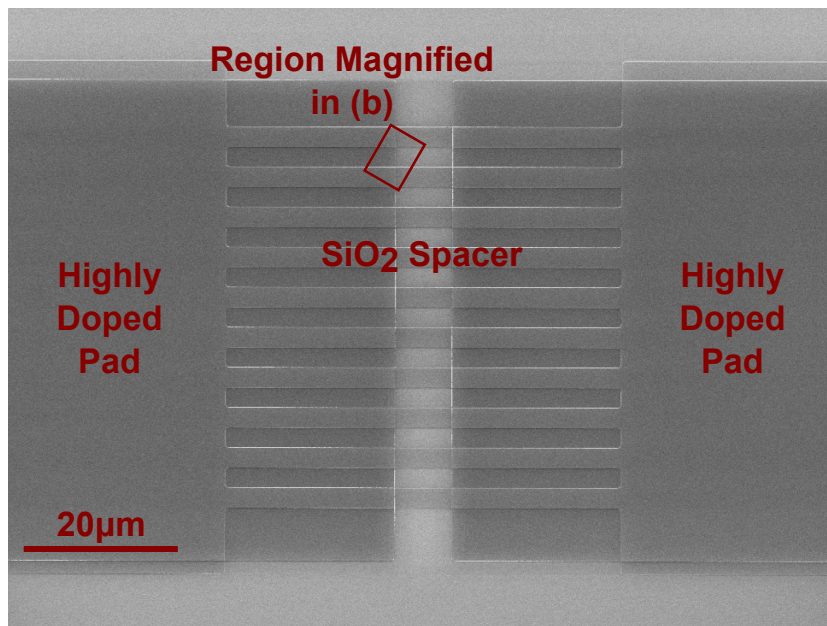
height and its dependence on the grain size, coupled with the density and distribution of GBIS in P-SiNW arrays. A wafer scale fabrication process enabled us to produce uniform P-SiNW arrays in the top down approach. The wires were characterized by Kelvin probe force microscopy and electrostatic TCAD simulations. This enabled us to find a good correlation between the grain size and the potential barrier height, showing a parabolic dependency, and extract the density of GBIS and their energy distribution within the band-gap.

2. Results and Discussion

A scanning electron microscope (SEM) micrograph of a typical NW array measured in this work is shown in Fig. 1. Figure 2, shows Kelvin probe force microscopy (KPFM) topography (black) and surface potential (red) images for the three studied samples, of a single P-SiNW grounded at both sides. The device shown is a $9\mu\text{m}$ long wire, with a $5\mu\text{m}$ long medium doped n region (which we term the ‘channel’), and two $2\mu\text{m}$ long highly doped n regions, one at each end (termed ‘source’ and ‘drain’ from left to right respectively). The KPFM measures the contact potential difference (CPD) which is defined as the work function difference between the AFM tip (Φ_{tip}) and a sample (Φ_{sample}) so that $CPD = -(\Phi_{tip} - \Phi_{sample})/q$ where q is an elementary charge.[19] Fig. 2 shows the excellent fit between the topography and the surface potential line profile along the P-SiNW for the 3 samples. We note here that the observed correlation between the topography and the surface potential was not seen on the surrounding surfaces, such as the oxide. We can therefore rule out the possibility of a cross-talk artifact as the origin of the observed correlation. Moreover, in case of measuring p-type P-SiNWs, the results show an accurate correlation between the topography and the CPD rather than the surface potential. We explain this correlation by considering the localized nature of charge accumulation at the GBs. As free charge carriers (electrons) are trapped at the GB region, a potential barrier is formed between two adjacent P-Si grains. This potential barrier induces band bending which is clearly seen in the measured surface potential. The GBIS density and energy distribution can be extracted from the measured potential by fitting it to electrostatic simulations. For this purpose, the simulation has to account for the P-SiNW’s geometry and GB locations, as well as for the doping density along the wire.

Throughout this work, we have used the Sentaurus device TCAD (*Synopsis Inc.*) to simulate the measured P-SiNW’s surface potential, locate the grain boundaries and extract the GBIS density and distribution. The NW’s shape was modeled first by introducing the measured topography line profile into the simulation without taking the GBs into account. Next, the 2D simulated topography profile was extruded along the angular direction by 90° to create a 3D quarter-of-a-cylinder resembling the NW, resting against two SiO_2 sidewall spacers as shown schematically in Fig. 3 (a). The cylinder mean radius was taken to be approximately 50 nm as measured by TEM radial cross section.

(a)



(b)

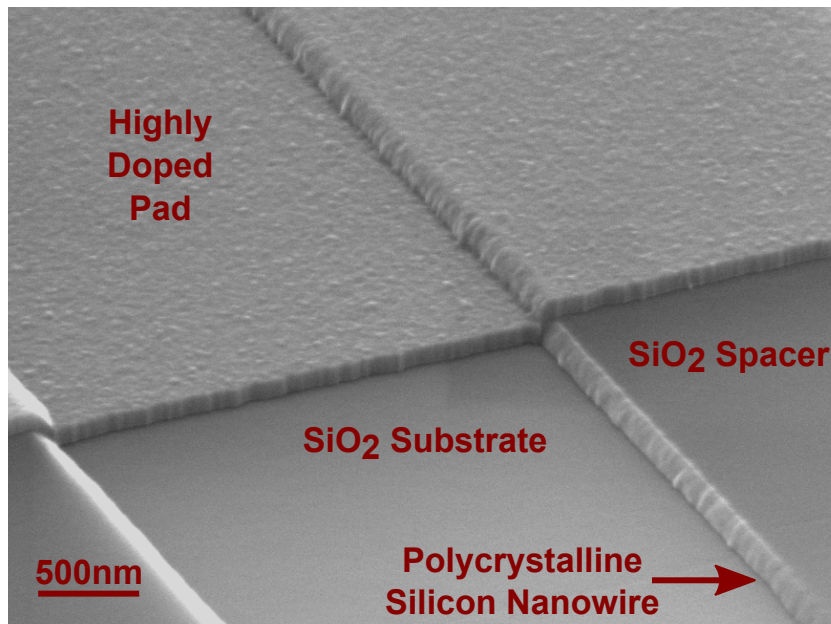


Figure 1. (a) SEM micrograph of the final architecture of the P-SiNW device array. The micrograph shows 10 oxide spacers stretching from one pad to another, forming an array of 20 nanowires. The magnified region (b) shows the P-SiNW resting against the SiO₂ spacer next to the source / drain pad region.

Splitting the bulk cylinder into individual grains requires adding a doping profile to the simulation, since the electrostatic behavior is determined by both the geometry

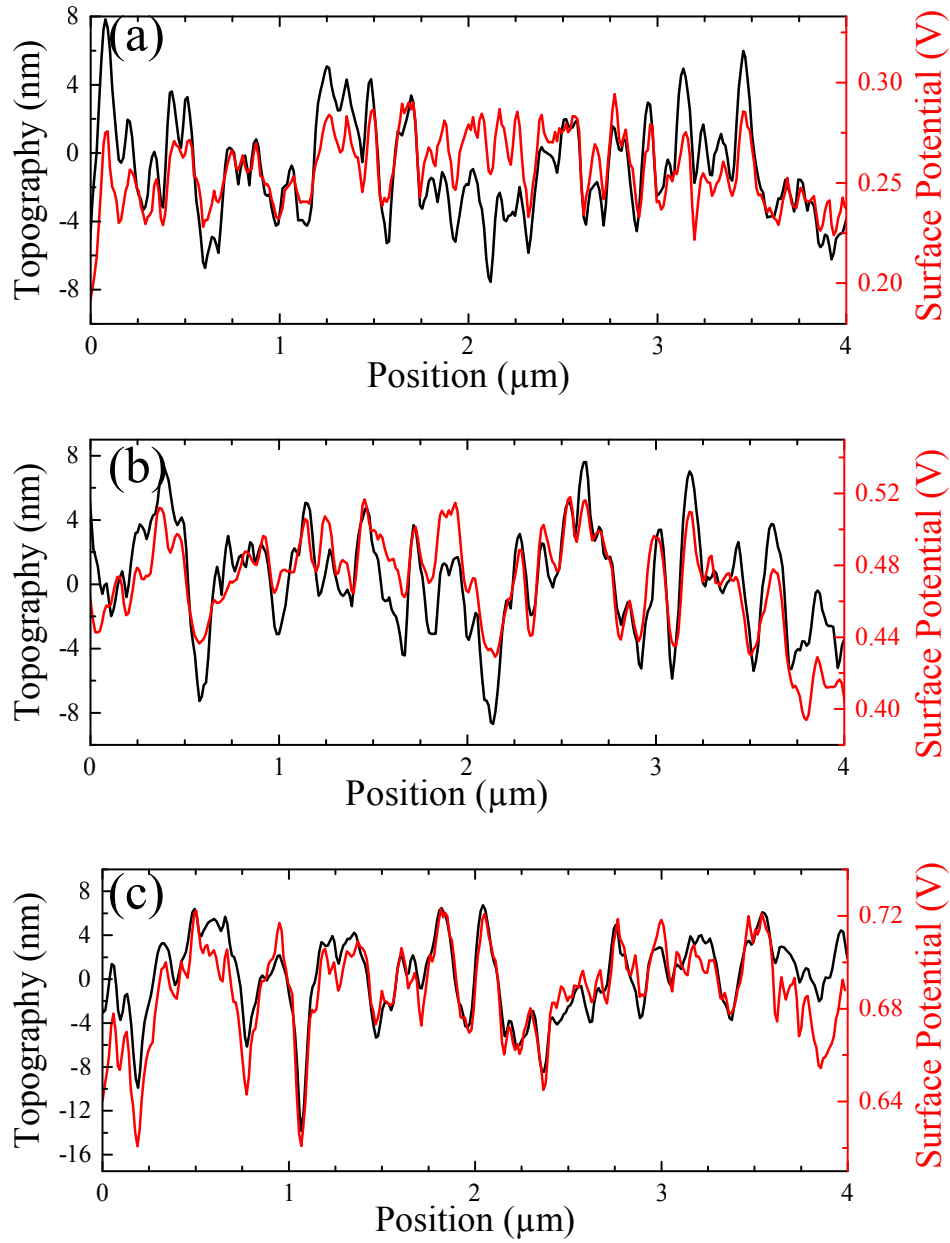


Figure 2. Topography (black curve) and surface potential (red curve) line profiles measured along the axial direction of P-SiNW of the samples A, B and C (a, b and c, respectively). Trapping states that are present at the grain boundaries are capable of trapping free charge carriers (electrons), become negatively charged, and therefore create a potential barrier between two adjacent Poly-Si grains.

and the doping of the grains. The radial doping profile was extracted from secondary ion mass spectroscopy (SIMS) performed on blank wafers that underwent the same treatment as the NWs. The SIMS measurement showed exponentially decaying doping profile, which was incorporated into the model using the following relation: $N_D(R) = N_0 \exp(R/21.7\text{nm})$, where R is the radial coordinate, with $R = 0$ at the center of the NW.

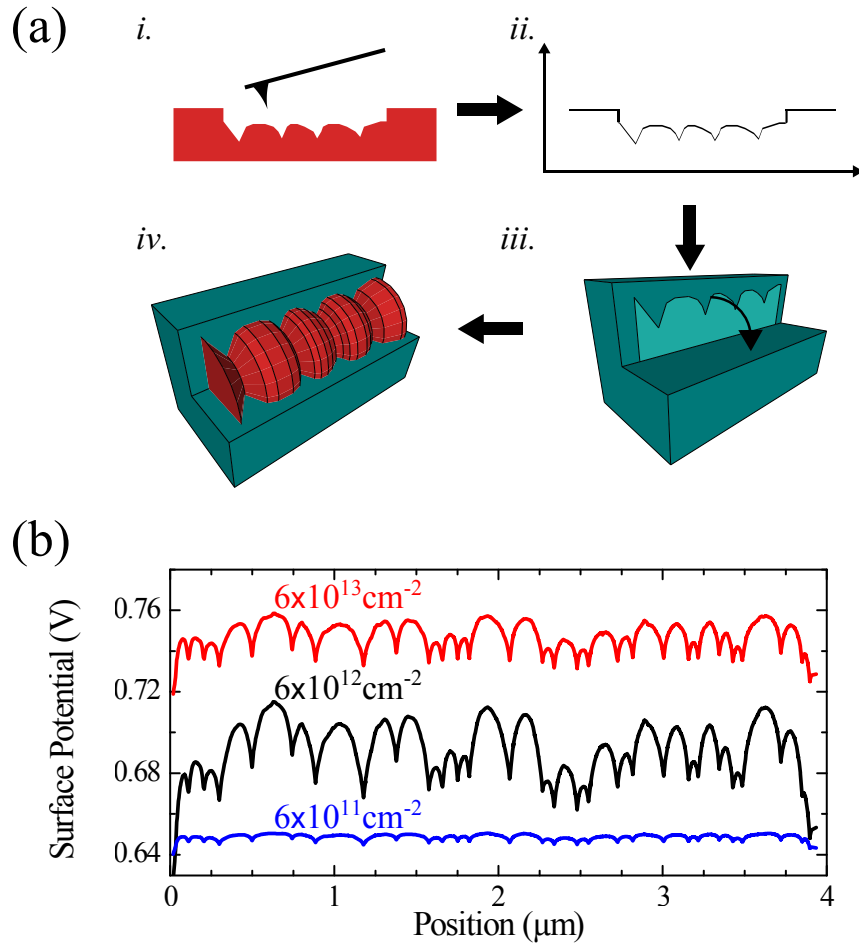


Figure 3. A schematic representation of the working steps: *i.* Measurement of the P-SiNWs topography; *ii.* Introducing the topography line profile into the simulator; *iii.* Extruding the 2D simulated topography profile along the angular direction by 90°; *iv.* The extruded 3D quarter-of-a-cylinder resembling the NW, resting against two SiO₂ spacers. (b) Surface potential line profiles from simulations corresponding to different trap concentration, measured along the axial direction of one of the P-SiNW samples. For the highest trap concentration (red curve) the GBIS concentration is higher than the carrier concentration, and therefore the crystallite is fully depleted of carriers and the traps are partially filled. For the lowest trap concentration (blue curve) the trapping states at the GBs are completely saturated and the bulk crystallites are only partially depleted.

With the doping profile incorporated into the simulation, we were able to determine the exact locations of each GB, by fitting it to the measured results. We note that not all of the deeps in the topographic profile are, in fact, GBs. Indeed, the average of several topographic profiles was needed to distinguish the actual topographic deeps from the noise. By introducing GBs into the 3D simulation and reiterating until the simulated results were in good agreement with the measured surface potential, the estimated locations of the GBs could be identified.

As a final simulation step, the GBIS concentration and distribution were changed in an iterative process, to produce the best fit to the measurements. In Fig. 3

(b), the black curve represents the surface potential line profile with the best fit to the measured surface potential profile. The two other curves represent simulation results for GBIS concentrations that are one order of magnitude larger (red curve) or smaller (blue curve) than the best fit. We note here that the potential barriers for the best fitted result are indicative of a very high trap concentration. For the highest simulated trap concentration (red curve), taking Seto's model into consideration, the GBIS concentration is higher than the carrier concentration, and therefore most of the crystallites are fully depleted of carriers and the traps are partially filled; whereas for the lowest trap concentration (blue curve) the GBIS are completely saturated and the bulk crystallites is only partially depleted. For both cases, the inherent potential barriers at the GBs are lower than the ones measured, and the best fit for the potential barrier height is at a GBIS concentration of $6 \times 10^{12} \text{cm}^{-2} \text{eV}^{-1}$ (black curve).

Previous works for bulk P-Si reported a 'U'-shape energy distribution of GBIS within the band gap, with different peak densities ranging from 4×10^{13} to $10^{14} \text{cm}^{-2} \text{eV}^{-1}$. [20, 21] A recently published paper by Amit *et al.*, [14] showed that this is the case in nanostructures as well. The acceptor and donor interface states were found to have a 'U'-shape distribution as described by the following expressions:

$$DOS_A = Q_t e^{-\left| \frac{E-E_C}{\sigma_0} \right|} \quad (1a)$$

$$DOS_D = Q_t e^{-\left| \frac{E-E_V}{\sigma_0} \right|} \quad (1b)$$

Where DOS_A and DOS_D are the acceptor and donor type interface states density and distribution, respectively. In this work, the GBIS were chosen to have a similar energy distribution with the same $\sigma_0 = 0.15 \text{eV}$, whereas the GBIS densities (Q_t) were those that best fitted the measured surface potential: $6 \times 10^{12} \text{cm}^{-2} \text{eV}^{-1}$, for samples A and C, and $8 \times 10^{12} \text{cm}^{-2} \text{eV}^{-1}$ for sample B. The results for the surface potential line profiles simulations and measurements of samples A, B and C, are presented in Fig. 4 a, b and c, respectively.

Having obtained the GBIS density and distribution, we now turn our attention to the influence of grain size on the resulting potential barrier at the GBs. Following Tsunekawa *et al.*, [22] the potential barrier height at individual GBs is defined by:

$$\Delta V_B = V_{Grain} - V_{GB} \quad (2a)$$

$$V_{GB} = \frac{V_{GB1} + V_{GB2}}{2} \quad (2b)$$

Where V_{Grain} and V_{GB} are the surface potential at the center of the measured grain and the average of the surface potential of the two adjoining grain boundaries, respectively. The potential barrier height is plotted in Fig. 5 (b) (black circles) as a function of the corresponding grain size for the three studied samples. The grain sizes that were extracted from KPFM measurements are an over estimation of the actual grain size, due to a tip-sample convolution and were corrected using a calibration factor found experimentally.

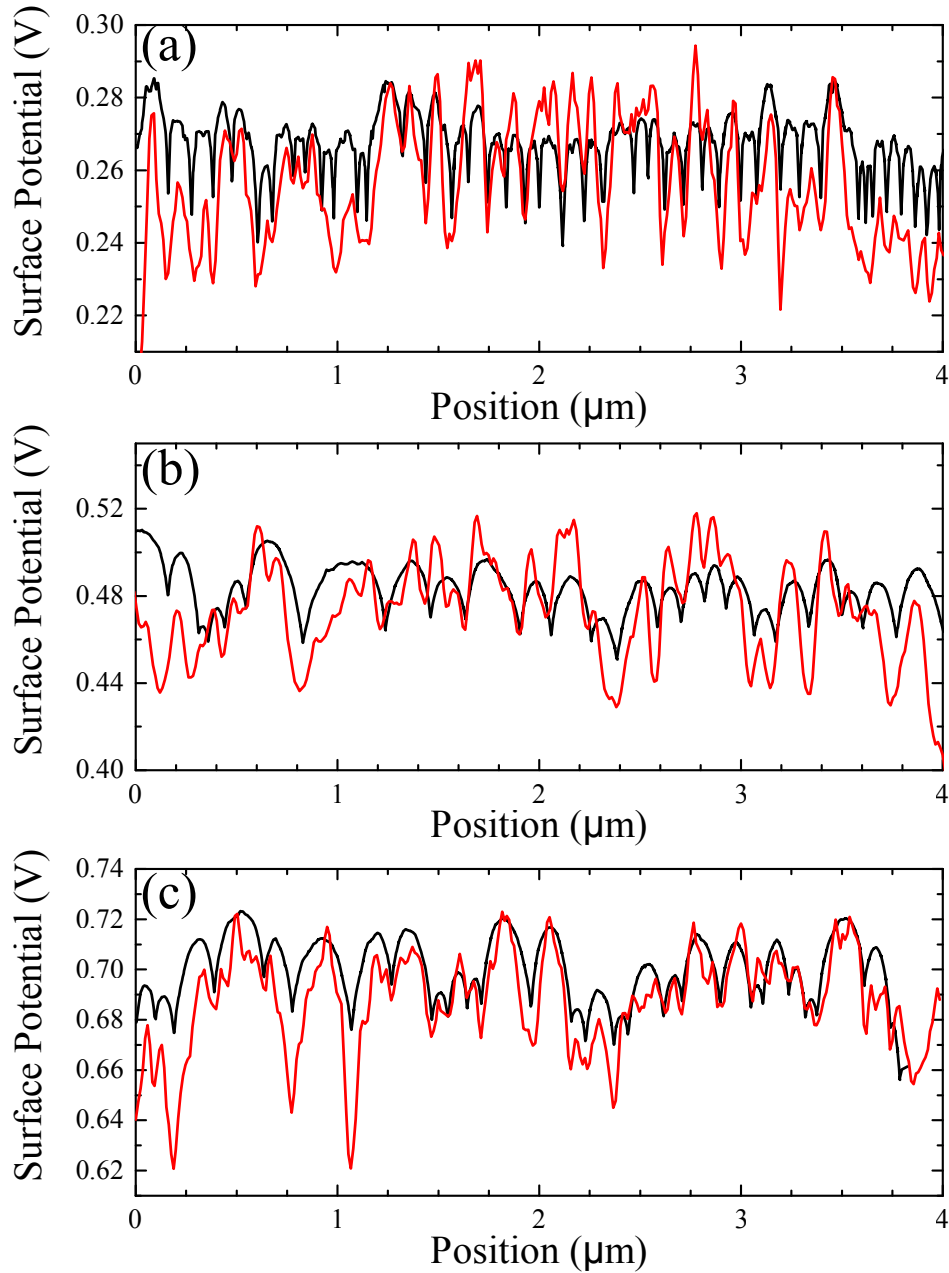


Figure 4. The measured surface potential (red curves) superimposed with the simulated surface potential (black curves) for samples A, B and C (a, b and c, respectively). The line profiles were taken along the axial direction of the P-SiNW.

Seto showed in his paper how the potential barrier height changes with respect to grain size and doping levels. To account for a more elaborate geometry, we have generalized Seto's model to three dimensions, taking the grains as perfect spheres, as opposed to a 1D grain, being accounted for in Seto's model: Our spherical grain has a radius R and donor doping density N . The GBIS at its surface have a density of Q_t at a single energy level, so that every single charge carrier is trapped in the GBIS until the traps are saturated. From symmetry considerations, the potential is assumed to be

invariant in the azimuthal and polar coordinates. Details of the model are shown in Fig. 5 (a).

Writing the Poisson equation in spherical coordinates under these assumptions yields:

$$\nabla^2 V = \frac{1}{r^2} \frac{\partial}{\partial r} \left(r^2 \frac{\partial V}{\partial r} \right) = -\frac{\rho}{\varepsilon} \quad (3)$$

At a critical radius R_c , there are just enough free charge carriers to saturate the traps and leave the grain fully depleted. From this equality, one can extract R_c to yield:

$$R_c = \frac{3Q_t}{N} \quad (4)$$

We therefore consider the model at two different regimes. The first, in which the grain is small enough, so that there are less charge carriers than GBIS resulting in a fully depleted grain ($R < R_c$). And the second case, in which the grain is bigger and therefore, the GBIS are fully saturated and the grain is only partially depleted ($R > R_c$). In the first case all of the free electrons in the grain are trapped at the GBIS, and hence, the charge density within the grain is simply $\rho = qN$. Maintaining the condition that the charge density on the surface of the grain should balance the volume charge completely, yields an interface states density of $\sigma = -RN/3$. Remembering that in Eq. 4 that the charge density is constant throughout the grain, the solution for the potential should be of the form of $V = Ar^2 + B$. Setting the potential at the center of the sphere ($r = 0$) to be zero, we can calculate the potential dependence on the radius inside the sphere:

$$V(r) = -\frac{qN}{6\varepsilon} r^2 \quad (5)$$

Finally, we see that the potential barrier height at the GB for electrons is given by:

$$V_B = -\Delta V(R) = \frac{qN}{6\varepsilon} R^2 \quad (6)$$

In the second case, the traps are saturated and the sphere is not fully depleted. We use the depletion approximation which states that the grain has a fully depleted shell, extending from the surface (the GB) to a certain depletion width, and is neutral at its core. The depletion width ($R - R_d$) is determined by balancing the charges on the surface and in the depletion region:

$$4\pi qN \int_{R_d}^R r^2 dr = 4\pi R^2 qQ_t \quad (7)$$

$$R_d = \left(R^3 - \frac{3R^2 Q_t}{N} \right)^{1/3} = \sqrt[3]{R^2(R - R_c)} \quad (8)$$

We can now write the charge density for the different regions in the sphere:

$$\rho = \begin{cases} 0 & r < R_d \\ qN & R_d < r < R \end{cases} \quad (9)$$

There is no net charge in the accumulated zone, and thus the potential at the grain's core is zero. In the depleted shell the Poisson equation is similar to Eq. 3. Here, however, we have to consider a solution of the type $V = Ar^2 + B + C/r$. Demanding that the electric field and the potential at the core-shell interface (R_d) will be zero, and solving for the potential we get:

$$V(r) = \begin{cases} 0 & r < R_d \\ -\frac{qN}{6\epsilon} \left(r^2 - 3R_d^2 + 2\frac{r_d^3}{r} \right) & R_d < r < R \end{cases} \quad (10)$$

Taking the potential at the edge of the grain, and substituting R_d with the expression found in Eq. 8, we can calculate the potential barrier height at the GB for electrons:

$$V_B = \frac{qN}{6\epsilon} \left(R^2 - 3 \left(R^2(R - R_c) \right)^{2/3} + 2R(R - R_c) \right) \quad (11)$$

At R_c both solutions are in agreement, reaching a maximum point of $V_B = qNR_c^2/6\epsilon$. It is evident from Fig. 5 (b), that the potential barrier, up to R_c , is monotonically increasing as a function of the grain size. The dependence can be fitted with a parabola applying for the first case of the model ($R < R_c$).

Fig. 5 (b) shows the comparison between our model (solid line), and the potential barrier height with respect to the grain size. The fitting parameter from Eq. 5 is the dopant concentration. This was evaluated, to a first approximation, from the measurements as was previously discussed, to increase by one order of magnitude, from $6.9 \times 10^{16} \text{cm}^{-3}$ at the interior of the NW to $6.9 \times 10^{17} \text{cm}^{-3}$ at the surface. The original modeled curve corresponds to a doping concentration of $1.5 \times 10^{16} \text{cm}^{-3}$, which is lower than expected. This discrepancy is explained with tip-sample convolution of the measurements, resulting in an overestimation of the grain sizes.

We take a linear dependence of the convolution of the probe on the measured grain size, a ‘‘convolution factor’’ can be estimated by comparison of the grain size distribution measured with KPFM to the one measured by TEM analysis. We find that a calibration factor of 4 attributed to the grain sizes measured yields a good fit. The calibrated results are presented in Fig. 5 (b) along with the modeled curve, and correlate to a doping concentration of $2.4 \times 10^{17} \text{cm}^{-3}$, which is in agreement with the measured doping concentration. The graph shows a remarkable agreement between our proposed model and the measured potential barrier height. Using this information, one can design, and fully control, the transport properties of P-Si devices by modulating both the grain sizes and doping profiles.

3. Conclusions

In summary, Kelvin probe force microscopy was used to measure top-down fabricated P-SiNW devices. Doping levels, as well as GBIS density and distribution were extracted by matching a single measurement to an electrostatic simulation. By considering a simplified electrostatic model, we have demonstrated the potential barrier height dependence on the poly-silicon grain size. The results show that there is a strong

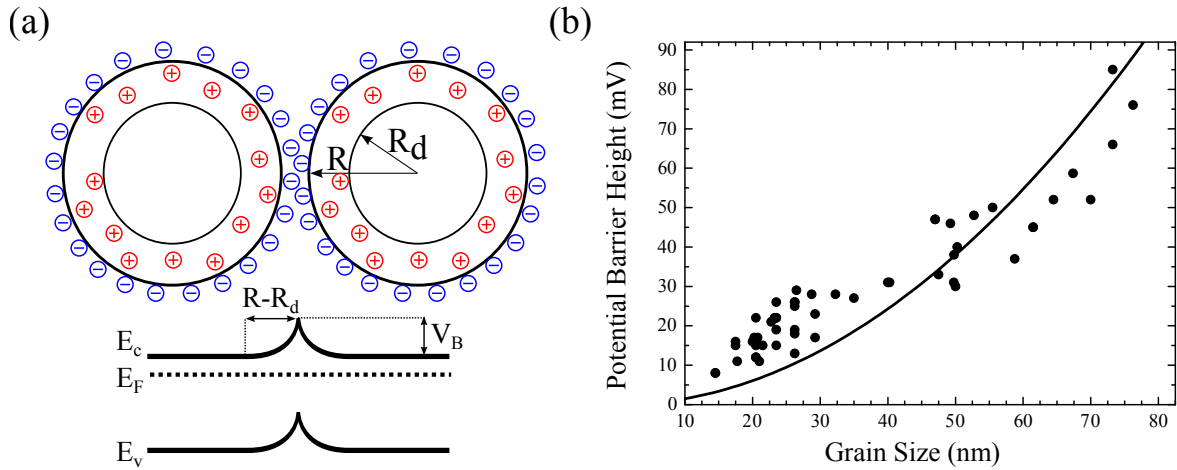


Figure 5. (a) A schematic representation of two spherical grains of a radius R . The GBIS are filled with negative trapped charge (marked in blue), resulting a positive depleted space charge region (marked in red), and the formation of a potential barrier height between the two adjacent grains. (b) Overlay of the measured potential barrier height with respect to the grain size, (black circles), and our proposed model (solid black line). The comparison shows good agreement between the model and the measured results.

correlation between the band structure and the topography inside the poly-silicon grains, indicating that the potential barriers formed between adjacent grains, could be measured directly, without relying on external assumptions. GBIS were found to have a ‘U’-shape energy distribution along the band gap with peak values of $6 \times 10^{12} \text{cm}^{-2} \text{eV}^{-1}$ for samples A and C, and $8 \times 10^{12} \text{cm}^{-2} \text{eV}^{-1}$ for sample B. The effect of the probe’s convolution on KPFM results is significant. Grains measured with KPFM deviate by an approximated factor of 4 than the ones measured by TEM analysis. According to our suggested model we concluded that the grain size of the samples is in the regime of $R < R_c$, meaning, that the trapping states concentration is higher than the carrier concentration, and thereby the crystallite is fully depleted of carriers (while the traps are partially filled), and that the potential barrier height (V_B) is proportional to the square of the grain radius.

4. Experimental Section

Fabrication of polysilicon nanowire arrays: The P-SiNWs in this work were fabricated using the side-wall spacer technique, described briefly by the following lithographic steps:[14] deposition of a P-Si layer on SiO_2 spacers, followed by the formation of the P-SiNWs using a dry etch process. Ion implantation was used to dope the wires with phosphorus atoms and form an n+-n-n+ structure. The final step included annealing the wafers to promote dopant activation. The grain sizes of the 3 studied samples (termed A, B and C) were modulated by adding different thermal treatments to samples B and C: Sample B underwent rapid thermal annealing (RTA) at 1050°C for 2 min. Sample C was annealed in a vertical diffusion furnace (VDF) at 1050°C for 120 min. Sample A

did not undergo any additional thermal treatments. The described fabrication process produced a matrix of NW arrays, varying both in the number of NWs per array and in NW's length.

KPFM measurements: The measurements were performed using a Dimension Edge AFM system (Bruker AXS) in a controlled nitrogen environment glove-box (less than 5 ppm H₂O). Measurements were conducted in the “dual-frequency mode”, where the topography is measured at the first mechanical resonance frequency of the cantilever in the “tapping mode”, and the CPD is measured electrically by exciting the tip at its first overtone frequency simultaneously. The probes used were highly doped silicon tips coated with Pt-Ir on both sides, with a nominal radius of curvature of 30 nm (Nanosensors, PPP-EFM). To facilitate the KPFM measurements, the P-SiNWs were electrically contacted by an additional lithographic step, and a deposition of 220 nm nickel contacts, which form Ohmic contacts to the source and the drain pads.

References

- [1] Lin, C.-H. *et al.* Poly-silicon nanowire field-effect transistor for ultrasensitive and label-free detection of pathogenic avian influenza DNA. *Biosensors and Bioelectronics* **24**, 3019–3024 (2009).
- [2] Stern, E. *et al.* Label-free immunodetection with CMOS-compatible semiconducting nanowires. *Nature* **445**, 519–522 (2007).
- [3] Gao, Z. *et al.* Silicon nanowire arrays for label-free detection of DNA. *Analytical Chemistry* **79**, 3291–3297 (2007).
- [4] Wu, C.-C. *et al.* Label-free biosensing of a gene mutation using a silicon nanowire field-effect transistor. *Biosensors and bioelectronics* **25**, 820–825 (2009).
- [5] Patolsky, F. & Lieber, C. M. Nanowire nanosensors. *Materials today* **8**, 20–28 (2005).
- [6] McAlpine, M. C. *et al.* High-performance nanowire electronics and photonics on glass and plastic substrates. *Nano Letters* **3**, 1531–1535 (2003).
- [7] Krogstrup, P. *et al.* Structural phase control in self-catalyzed growth of GaAs nanowires on silicon (111). *Nano letters* **10**, 4475–4482 (2010).
- [8] Mandl, B. *et al.* Growth Mechanism of Self-Catalyzed Group III- V Nanowires. *Nano letters* **10**, 4443–4449 (2010).
- [9] Cui, Y., Wei, Q., Park, H. & Lieber, C. M. Nanowire nanosensors for highly sensitive and selective detection of biological and chemical species. *Science* **293**, 1289–1292 (2001).
- [10] Li, Z. *et al.* Sequence-specific label-free DNA sensors based on silicon nanowires. *Nano Letters* **4**, 245–247 (2004).
- [11] Demami, F., Pichon, L., Rogel, R. & Salaün, A.-C. Fabrication of polycrystalline silicon nanowires using conventional UV lithography. In *IOP Conference Series: Materials Science and Engineering* vol. 6 012014, (IOP Publishing2009).
- [12] Chang, C.-W., Deng, C.-K., Chang, H.-R., Chang, C.-L. & Lei, T.-F. A simple spacer technique to fabricate poly-Si TFTs with 50-nm nanowire channels. *Electron Device Letters, IEEE* **28**, 993–995 (2007).
- [13] Wu, C.-Y. *et al.* Electrical characterization of field-enhanced poly-Si nanowire SONOS memory. In *VLSI Technology Systems and Applications (VLSI-TSA), 2010 International Symposium on* 61–62, (IEEE2010).
- [14] Amit, I., Englander, D., Horvitz, D., Sasson, Y. & Rosenwaks, Y. Density and Energy Distribution of Interface States in the Grain Boundaries of Polysilicon Nanowire. *Nano letters* **14**, 6190–6194 (2014).

- [15] Hsiao, C.-Y. *et al.* Novel poly-silicon nanowire field effect transistor for biosensing application. *Biosensors and Bioelectronics* **24**, 1223–1229 (2009).
- [16] Wenga, G. *et al.* Step-gate polysilicon nanowires field effect transistor compatible with CMOS technology for label-free DNA biosensor. *Biosensors and Bioelectronics* **40**, 141–146 (2013).
- [17] Hakim, M. M. *et al.* Thin film polycrystalline silicon nanowire biosensors. *Nano letters* **12**, 1868–1872 (2012).
- [18] Seto, J. Y. The electrical properties of polycrystalline silicon films. *Journal of Applied Physics* **46**, 5247–5254 (1975).
- [19] Rosenwaks, Y., Shikler, R., Glatzel, T. & Sadewasser, S. Kelvin probe force microscopy of semiconductor surface defects. *Physical Review B* **70**, 085320 (2004).
- [20] De Graaff, H., Huybers, M. & De Groot, J. Grain boundary states and the characteristics of lateral polysilicon diodes. *Solid-State Electronics* **25**, 67–71 (1982).
- [21] Fortunato, G. & Migliorato, P. Determination of gap state density in polycrystalline silicon by field-effect conductance. *Applied physics letters* **49**, 1025–1027 (1986).
- [22] Tsurekawa, S., Kido, K. & Watanabe, T. Measurements of potential barrier height of grain boundaries in polycrystalline silicon by Kelvin probe force microscopy. *Philosophical magazine letters* **85**, 41–49 (2005).

Supporting information:

**Grain Boundary Characterization and
Potential Barrier Height Dependence on
Grain Size in Poly-Silicon Nanowire**

*Assaf Shamir, Iddo Amit, Danny Englander, Dror Horvitz, and Yossi Rosenwaks**

Department of Physical Electronics, School of Electrical Engineering, Tel-Aviv

University,

Ramat-Aviv 69978, Israel.

The complete analytical electrostatic model

We present an electrostatic model for the relation between the potential barrier height and the grain size in the GBs of the P-SiNWs. Seto showed in his paper how the potential barrier height changes with respect to grain size and doping levels. To account for a more elaborate geometry, we have generalized Seto's model to three dimensions, taking the grains as perfect spheres, as opposed to a 1-D grain, being accounted for in Seto's model: Our spherical grain has a radius R and donor doping density N . The GBIS at its surface have a density of Q_t at a single energy level, so that every single charge carrier is trapped in the GBIS until the traps are saturated.

We use the Poisson equation in spherical coordinates:

$$(1) \quad \nabla^2 V = -\frac{\rho}{\varepsilon}$$

Where $\nabla^2 V$ in spherical coordinated is given by:

$$(2) \quad \nabla^2 V = \frac{1}{r^2} \frac{\partial}{\partial r} \left(r^2 \frac{\partial V}{\partial r} \right) + \frac{1}{r^2 \sin \theta} \frac{\partial}{\partial \theta} \left(\sin \theta \frac{\partial V}{\partial \theta} \right) + \frac{1}{r^2 \sin^2 \theta} \left(\frac{\partial V}{\partial \phi} \right)$$

From symmetry considerations, the potential is assumed to be invariant in the azimuthal and polar coordinates (i.e. $\partial V / \partial \theta = 0$ and $\partial V / \partial \phi = 0$), which leaves us with:

$$(3) \quad \nabla^2 V = \frac{1}{r^2} \frac{\partial}{\partial r} \left(r^2 \frac{\partial V}{\partial r} \right) = -\frac{\rho}{\varepsilon}$$

At the critical radius R_c , the trapping states are completely populated, and balanced by the static charges of the donor atoms:

$$(4) \quad \frac{4}{3} \pi R_c^3 q N + 4 \pi R_c^2 q Q_t = 0$$

From this equality, one can extract R_c to yield:

$$(5) \quad R_c = \frac{3Q_t}{N}$$

We therefore consider the model at two different regimes. The first, in which the grain is small enough, so that there are less charge carriers than GBIS resulting in a fully depleted grain ($R < R_c$). And the second case, in which the grain is bigger and therefore, the GBIS are fully saturated and the grain is only partially depleted ($R > R_c$). In the first case all of the free electrons in the grain are trapped at the GBIS, and hence, the charge density within the grain is simply $\rho = qN$ and Eq. 4 becomes:

$$(6) \quad \frac{4}{3} \pi R^3 qN + 4\pi R^2 q\sigma = 0$$

Maintaining the condition that the charge density on the surface of the grain should balance the volume charge completely, yields an interface states density of:

$$(7) \quad \sigma = -\frac{RN}{3}$$

In Eq. 7, we see that the charge density is constant throughout the sphere, and therefore the solution should have the form $V = Ar^2 + B$. Taking the derivative:

$$(8) \quad \nabla^2 V = \frac{1}{r^2} \frac{\partial}{\partial r} \left(r^2 \frac{\partial}{\partial r} (Ar^2 + B) \right) = 6A = -\frac{qN}{\epsilon}$$

Which means that the first coefficient is $A = -qN/6\epsilon$. We set the potential at the center of the sphere ($r=0$) to be zero (so that $B=0$) and obtain:

$$(9) \quad V(r) = -\frac{qN}{6\epsilon} r^2$$

And the electric field within the sphere:

$$(10) \quad E = -\frac{\partial V}{\partial r} = \frac{qN}{3\epsilon} r$$

The interface charge density dictates that the electric field outside the sphere should vanish:

$$(11) \quad \epsilon(E_{out} - E_{in}) = q\sigma$$

Substituting the electric field and interface state density from Eq. 10 and 7 we obtain:

$$(12) \quad E_{out} = \frac{q\sigma}{\epsilon} + E_{in} = -\frac{qNR}{3\epsilon} + \frac{qNR}{3\epsilon} = 0$$

Finally, we can see the potential barrier height at the GB for electrons is given by:

$$(13) \quad V_B = -\Delta V(R) = \frac{qN}{6\epsilon} R^2$$

In the second case ($R > R_c$), the traps are saturated and the sphere is not fully depleted.

We use the depletion approximation which states that the grain has a fully depleted shell, extending from the surface (the GB) to a certain depletion width, and is neutral at its core. The depletion width ($R - R_d$) is determined by balancing the charges on the surface and in the depletion region:

$$(14) \quad 4\pi qN \int_{R_d}^R r^2 dr = 4\pi R^2 qQ_t$$

$$(15) \quad R_d = \left(R^3 - \frac{3R^2 Q_t}{N} \right)^{1/3} = \sqrt[3]{R^2(R - R_c)}$$

We can now write the charge density within the different regions in the sphere:

$$(16) \quad \rho = \begin{cases} 0 & r < R_d \\ qN & R_d < r < R \end{cases}$$

In the accumulated zone there is no net charge, and thus the potential is zero. In the depleted region the Poisson equation is again as follows:

$$(17) \quad \frac{1}{r^2} \frac{\partial}{\partial r} \left(r^2 \frac{\partial V}{\partial r} \right) = -\frac{qN}{\epsilon}$$

Here, however, we have to consider a solution of the type $V = Ar^2 + B + C/r$. The solution for the first coefficient again is $A = -qN/6\epsilon$. Assuming that the electric field at R_d is zero:

$$(18) \quad E(R_d) = \left(\frac{\partial \left(-\frac{qN}{6\epsilon} r^2 + B + C/r \right)}{\partial r} \right) = \frac{qN}{3\epsilon} R_d + \frac{C}{R_d^2} = 0$$

$$(19) \quad C = -\frac{qN}{3\epsilon} R_d^3$$

Next, we assume that the potential at R_d will be zero and extract the second coefficient

B:

$$(20) \quad V(R_d) = -\frac{qN}{3\epsilon} R_d^2 + B - \frac{qN}{3\epsilon} \frac{R_d^3}{R_d} = 0$$

$$(21) \quad B = \frac{qN}{2\epsilon} R_d^2$$

And finally, solving for the potential we get:

$$(22) \quad V(r) = \begin{cases} 0 & r < R_d \\ -\frac{qN}{6\epsilon} \left(r^2 - 3R_d^2 + 2\frac{R_d^3}{r} \right) & R_d < r < R \end{cases}$$

The charges on the surface cause a discontinuity in the electric field at R :

$$(23) \quad E_{in}(R) = \frac{qN}{3\epsilon} \left(2R - \frac{R_d^3}{R^2} \right)$$

Substituting R_c with the expression in Eq. 5 gives:

$$(24) \quad \epsilon E_{in}(R) = qQ_t$$

Which satisfies the condition for the surface charge density, and therefore it's easy to see that the field outside the sphere vanishes. Taking the potential at the edge of the grain, we can calculate the potential barrier height at the GB for electrons:

$$(25) \quad V_B = -\Delta V(R) = \frac{qN}{6\epsilon} \left(R^2 - 3R_d^2 - \frac{R_d^3}{R} \right)$$

Substituting the expression once again for R_d with the one we found:

$$(26) \quad V_B = \frac{qN}{6\epsilon} \left(R^2 - 3(R^2(R - R_c))^{2/3} + 2R(R - R_c) \right)$$

At R_c both solutions are in agreement, reaching a maximum of $V_{B_{\max}} = 3qQ_t^2/2\epsilon N$.